

A first comparison of TROPOMI ALH to CALIOP data

Swadhin Nanda², Martin de Graaf¹, J. Pepijn Veeftkind^{1,2}, Maarten Sneep¹, Mark ter Linden^{1,3}, Jiyunting Sun^{1,2}, and Pieternel F. Levelt^{1,2}

¹Royal Netherlands Meteorological Institute (KNMI), Utrechtseweg 297, 3731 GA De Bilt, The Netherlands

²Delft university of Technology (TU Delft), Mekelweg 2, 2628 CD Delft, The Netherlands

³S&T Corp, Delft, The Netherlands

Correspondence to: Swadhin Nanda (s.nanda@tudelft.nl)

Abstract. The Tropospheric Monitoring Instrument's (TROPOMI) level-2 aerosol layer height (ALH) product has now been released to the general public. This product is retrieved using TROPOMI's measurements of the oxygen A-band, radiative transfer model (RTM) calculations augmented by neural networks and an iterative optimal estimation technique. The TROPOMI ALH product will deliver ALH estimates over cloud-free scenes over the ocean and land that contain aerosols above a certain threshold of the measured UV aerosol index (UVAI) in the ultraviolet region. This paper provides background for the ALH product and explores its quality by comparing ALH estimates to similar quantities derived from spaceborne LIDARs observing the same scene. The spaceborne LIDAR chosen for this study is the Cloud-Aerosol LIDAR with Orthogonal Polarisation (CALIOP) on board the Cloud-Aerosol LIDAR and Infrared Pathfinder Satellite Observations (CALIPSO) mission, which flies in formation with NASA's A-train constellation since 2006 and is a proven source of data for studying ALHs. The influence of the surface and clouds are discussed and the aspects of the TROPOMI ALH algorithm that will require future development efforts are highlighted.

A case-by-case analysis of the data from the four selected cases (mostly around the Saharan region with approximately 800 colocated TROPOMI pixels and CALIOP profiles in Jun and December of 2018) shows that ALHs retrieved from TROPOMI using the operational Sentinel-5 Precursor Level-2 ALH algorithm is lower than CALIOP aerosol extinction heights by approximately 0.5 km. Looking at data beyond these cases, it is clear that there is a significant difference when it comes to retrievals over land, where these differences can easily go over 1 km on average.

1 Introduction

Aerosols are an important component of the Earth system which provide the means for the formation of clouds by acting as cloud-condensation nuclei, affecting the Earth's radiation budget by absorbing or scattering incoming solar radiation (Twomey, 1974), and even nurturing forests from across oceans (Yu et al., 2015; Barkley et al., 2019). A significant source of origin for aerosols is natural, followed by anthropogenic contribution to the Earth's atmosphere. The IPCC (2014) report has made it clear that the current scientific consensus acknowledges the impact of aerosols on the Earth's radiation budget via direct, indirect and semi-direct effects. What makes monitoring aerosols difficult is the high spatial and temporal variability of aerosol micro and macrophysical properties (Li et al., 2009). To that extent, there are several spaceborne, ground-based and airborne

missions extensively monitoring these aerosol micro and macrophysical properties. These missions aim to reduce the gaps in our knowledge of aerosol radiative effects by accurately measuring aerosol properties at a high spatial and temporal resolution. This paper specifically discusses retrieving information on the vertical distribution of aerosol layer in the atmosphere, which has significant relevance in deriving auxiliary aerosol properties and subsequently understanding aerosol radiative effects (ARE), primarily absorption of radiation by aerosols. Torres et al. (1998) explicitly mention the importance of knowledge about aerosol vertical distribution which can be used in tandem with the UV aerosol index (UVAI) to compute aerosol properties such as AOT (AOT) and effective single scattering albedo over cloud-free and snow-free scenes. de Graaf (2005) provide several sensitivity analyses that detail the importance of the aerosol height in interpreting the UVAI. Sun et al. (2018) explicitly mention in their study the requirement of accurate aerosol layer height (ALH) estimates in order to derive aerosol absorption from the UVAI.

The global monitoring of aerosol properties can only be done using remote sensing techniques from space. The space-based techniques currently utilised by the scientific community to retrieve aerosol vertical information are divided into two categories — active and passive techniques; active remote sensing techniques monitor aerosol properties by measuring the interaction of energy generated by the instrument with aerosols in the atmosphere, whereas passive techniques do the same by measuring the interaction of natural light with aerosol particles. There are several differences in the sensing principles between active and passive remote sensing of aerosols, specifically in terms of vertical resolution. Active sensors such as the CALIOP instrument provide attenuated backscatter profiles resolved vertically at a vertical resolution as fine as 30 m for different channels over a spatial resolution as fine as 0.33 km (see Table 2 of Winker et al. (2009)). While these measured backscatter profiles provide detailed quantitative information on the scattering components present in the atmosphere, spaceborne atmospheric profiling LIDARs have limited spatial coverage due to their limited beam width. Owing to this particular feature of active remote sensing, spaceborne LIDARs currently do not revisit a specific point on Earth several times a day, or even on a daily basis. On the other hand, passive spaceborne remote sensing has the ability to measure a specific point on Earth once a day for polar orbiting satellite missions and several times in the day for geostationary missions. Currently however, the retrieved information on aerosol vertical distribution from passive remote sensing techniques is much more limited when compared to active techniques such as orbiting LIDARs.

Several passive retrieval strategies that are either currently in their operational phase or are upcoming remote sensing missions utilise the interaction of incoming solar radiation with the aerosol particles to retrieve height information. Some notable mentions of missions that retrieve ALH are Multiangle Imaging Spectroradiometer (MISR) on board the NASA Terra satellite (Nelson et al., 2013) which measures aerosol height using geometric optics, the Deep Space Climate Observatory (DSCOVR) mission with its Earth Polychromatic Imaging Camera (EPIC) (Xu et al., 2017, 2019), the Ozone Monitoring Instrument (OMI) on board the NASA Aura mission (Chimot et al., 2017, 2018; Choi et al., 2019), and finally the TROPOMI instrument on board the Sentinel-5 Precursor mission (Veefkind et al., 2012). Xu et al. (2017) and Xu et al. (2019) are the first study to demonstrate that the diurnal cycle of aerosol height is retrievable. In the near future, missions like the upcoming Multi-Angle Imager for Aerosols (MAIA) mission (Davis et al., 2017), the Geostationary Environment Monitoring Spectrometer (GEMS) (Kim et al., 2019), Sentinel-4, Sentinel-5 (Ingmann et al., 2012) and the Tropospheric Emissions: Monitoring Pollution mission (TEMPO) (Zoogman et al., 2017) are expected to provide aerosol height retrievals as well (Kim et al., 2018; Park et al., 2016; Zoog-

man et al., 2017). These instruments are examples of missions demonstrably (some theoretically, others practically) capable of retrieving ALH. Except for TROPOMI however, there are currently no passive remote sensing mission that provides an operational stream of retrieved ALHs. In the fourth quarter of 2019, an operational data stream of retrieved ALHs derived from measured oxygen A-band spectra by TROPOMI has been made available to the general public; the TROPOMI operational UVAI product augmented by the TROPOMI ALH product has the potential to further the operational monitoring of aerosol properties globally. This paper discusses some key features of the product and its limitations by comparing it with co-located CALIOP profiles, and paints a future outlook of the evolution of the TROPOMI ALH algorithm. The paper looks into more than two million colocations between TROPOMI ground pixels and CALIOP profiles over an extended period of time covering several months from May 2018 till March 2019, in order to draw conclusions on the accuracy of the TROPOMI ALH retrievals. Further on, the paper also discusses four selected cases in and around West Africa for a deeper analysis of the comparison with CALIOP data; the choice of using the Africa as a study area arises from the fact that a significant majority of colocations between TROPOMI and CALIOP are concentrated around the West African region.

In Section 2) of this paper, we discuss the data and methods used in this paper; Section 2.1 describes the retrieval algorithm and highlights different diagnostic parameters available for assessing the product's quality. Following this, the comparison between CALIOP and TROPOMI estimates of aerosol heights are presented in Section 3 — Section 3.1 presents an overall analysis of a large number of TROPOMI-CALIOP colocations, followed by Section 3.2 which discusses selected cases for a deeper dive into the TROPOMI product. The paper concludes with Section 4, highlighting important areas of potential improvement in the current TROPOMI ALH product.

2 Data and Methods

2.1 TROPOMI ALH

The TROPOMI ALH product is derived from measurements of the oxygen A-band in the near infrared region between 758 nm and 770 nm. Within this spectral range, TROPOMI measures top of atmosphere radiances and solar irradiances with a spectral resolution between 0.34 nm and 0.35 nm and a spectral sampling of 0.126 nm. The retrieval algorithm exploits the absorption characteristics of molecular oxygen, which varies with the photon path length — the photon path length for an aerosol layer closer to the surface is longer, which appears as deeper oxygen absorption lines in the measured spectrum (see Figure 1 of Nanda et al. (2018a)).

The reported ALH is the height of a single aerosol layer for the entire atmospheric column within the scene measured by TROPOMI; in reality however, there can be several cases where distinctly separated elevated and boundary layer aerosols are present in the same scene. In such cases, the retrieval algorithm is expected to retrieve an optical centroid pressure or height of the two (or more) aerosol layers, depending on the atmospheric level of the aerosol layer from which most of the photons are scattered back. For instance, if the elevated aerosol layer contributes significantly more than the boundary layer aerosols to the top of atmosphere measured spectra, the ALH retrieval algorithm is expected to retrieve values closer to the elevated layer.

The technique for retrieving ALH is based on optimal estimation (Rodgers, 2000), where an RTM that calculates the top of atmosphere oxygen A-band spectra is fitted to TROPOMI measured oxygen A-band spectra. The cost function that is minimised in this estimation step, χ^2 , is defined as

$$\chi^2 = [\mathbf{y} - \mathbf{F}(\mathbf{x}, \mathbf{b})]^T \mathbf{S}_\epsilon^{-1} [\mathbf{y} - \mathbf{F}(\mathbf{x}, \mathbf{b})] + (\mathbf{x} - \mathbf{x}_a)^T \mathbf{S}_a^{-1} (\mathbf{x} - \mathbf{x}_a), \quad (1)$$

5 where, \mathbf{y} is the reflectance spectra calculated from measured radiances and irradiances for the oxygen A-band, $\mathbf{F}(\mathbf{x}, \mathbf{b})$ is the modeled reflectance for input parameters \mathbf{b} , of which the state vector \mathbf{x} containing ALH z_{aer} and AOT τ is a part, \mathbf{x}_a is the a priori state vector and \mathbf{S}_ϵ^{-1} and \mathbf{S}_a^{-1} are the measurement error covariance and the a priori error covariance matrices. Optimal estimation is an iterative process, requiring several iterations to minimise the cost function described in Equation 1. The approach is Gauss-Newton, with a maximum number of iterations set at 10. If the optimal estimation does not converge
 10 within these iterations, the ALH field in the final level-2 product is filled with a fill value. For a given measurement, optimal estimation is said to have converged to a final solution if the update to the state vector for the next iteration is less than the expected precision.

The χ^2 is a measure of how close the modelled sun-normalised radiances are to the observations, with smaller values representing a better fit. The consequence of the many assumptions in the model (described in Section 2.2 of Nanda et al.
 15 (2019)) result in a large χ^2 (to the order of 1×10^4 - 1×10^7), with larger χ^2 representing a larger departure between the model and the observation. There are several reasons for these departures, the more important ones being the presence of undetected clouds in the scene, incorrect surface reflectance information, and multiple aerosol layers. These attributes are not parameterised into the RTM, and can be source of discrepancies between the measured and the modeled reflectances. The RTM in this case is a neural network model that has learned parts of a full physics RTM derived from de Haan et al. (1987) called Determining
 20 Instrument Specifications And Methods for Atmospheric Retrievals (DISAMAR, described in Section 3 of Nanda et al. (2019)), which is three orders of magnitude faster than DISAMAR. In short, the atmosphere is simplified by DISAMAR in order to reduce computational burden, and the neural network forward model is implemented for a further performance boost in an operational environment; for instance, DISAMAR ignores rotational raman scattering even though literature has shown that the oxygen A-band ring effects are sensitive to ALH (Vasilkov et al., 2013; Wagner et al., 2010). These decisions have been
 25 made in order to speed up line-by-line calculations of DISAMAR, which are the basis of the training data for its neural network counterpart. This decision is motivated by preliminary sensitivity analyses conducted by Sanders and de Haan (2016) which conclude that the effect of ignoring RRS is not significant enough to venture in its implementation into the forward model.

The surface reflectance model used in the algorithm is derived from Tilstra et al. (2017), which is a Lambertian equivalent reflectance (LER) database with a spatial resolution of $0.25^\circ \times 0.25^\circ$. In contrast to TROPOMI's ALH product which is
 30 reported at $7.2 \text{ km} \times 3.6 \text{ km}$ till August 6, 2019, and $5.6 \text{ km} \times 3.6 \text{ km}$ thereafter, the LER database is much coarser spatially. This can lead to several artefacts in the final product, discussed further on in this paper in Section 3.2. Another issue to note is in the influence of bright surfaces on the retrieval. The oxygen A-band lies beyond the red edge, a wavelength region in which vegetation has high reflectance values. This poses several challenges; a significant portion of the measured signal over land

might be contributions from the surface reflectance (see Figure 3 from Nanda et al. (2018a)). If the AOT of the measured scene is low, the contribution of the surface to the top of atmosphere radiance dominates over the contribution from scattering by aerosols — there are more photons that get scattered back from the surface than the aerosol layer. In such cases, the retrieval algorithm will tend to retrieve an aerosol layer closer to the surface. Generally we find that, if the contribution to the top
5 of atmosphere reflectance from aerosols is significantly larger than the same from the surface (i.e. the aerosol layer appears brighter than the surface), the retrieval algorithm will tend to retrieve a height closer to the aerosol layer (Section 5.2 and Figure 10 from Nanda et al. (2018b) discuss this observation explicitly).

The forward model parameterises aerosols with a Henyey-Greenstein scattering phase function (Henyey and Greenstein, 1941) with an asymmetry factor of 0.7, a single scattering albedo of 0.95, and a fixed AOT for an aerosol layer parameterised
10 by a single atmospheric layer with a 50 hPa thickness. These assumptions have to be made since very little a priori information about aerosols in a scene is known. While more complex scattering models exist, the Henyey-Greenstein model has been used for retrieving ALH when the forward model was of line-by-line nature as the number of calculations it requires is far less than a scattering model such as the Mie model (de Rooij and van der Stap, 1984). Sensitivity analyses have shown that this assumption has few ramifications (Sanders et al., 2015). Fixing the single scattering albedo is a much bigger concern; while
15 retrievals over the ocean do not suffer for a priori errors in the single scattering albedo, retrievals over land do have large errors and non-convergences which reduce as the the viewing zenith angle increases (Nanda et al., 2018a). The choice of using 0.95 as a fixed value arises from average values derived by Dubovik et al. (2002) from long-term observations using the aerosol robotic network (AERONET, Holben et al. (1998)). The algorithm assumes a single aerosol layer for the entire atmosphere, within which aerosols are uniformly distributed and the aerosol volume extinction coefficient is constant. This is an important
20 simplification to note when comparing with CALIOP profiles, since these LIDAR profiles have the capability to detect multiple aerosol layers. The simplicity in the aerosol profile parameterisation arises from the fact that it is impossible to know, without prior information, whether the scene consists of a single or multiple aerosol layers. While fitting of the aerosol layer pressure thickness along with the aerosol layer mid pressure does not result in large errors in the retrieved ALH, the precision of the retrieved aerosol layer mid pressure significantly deteriorates with increasing errors in the surface albedo (Sanders et al., 2015).
25 More research has to be done before more information on the aerosol profile is retrieved from the oxygen A-band alone.

Finally, the ALH retrieval algorithm implements a pixel selection scheme before committing to retrieving ALH estimates. This pixel selection scheme involves auxiliary data products from TROPOMI such as the UVAI (www.tropomi.eu/document/atbd-uv-aerosol-index) and cloud fraction estimates from the TROPOMI Fast Retrieval Scheme for Clouds from Oxygen absorption bands (FRESCO) algorithm (Wang et al., 2008), and the cirrus reflectances derived from the Visible Infrared Imaging
30 Radiometer Suite (VIIRS) on the Suomi National Polar-Orbiting Partnership (Suomi NPP) satellite.

1. The maximum solar zenith angle allowed is 75° . If the pixel does not meet this criterion, it is removed from the processing and a flag is raised.
2. If the pixel over water lies in the sun-glint region (a maximum sun-glint angle of 18°), it is processed but a sun glint warning flag is recorded in the level-2 product.

3. If the standard deviation of the surface elevation within the pixel is beyond 1000 m, the pixel is not processed and a flag is raised. If it is beyond 300 m, a warning flag is raised and the pixel is processed.
4. If the surface covered by the pixel comprises of both land and water, a warning indicating mixed surface type is raised and the pixel is processed regardless.
5. If the pixel contains snow or ice, the pixel is not processed and a flag is raised.
6. If the TROPOMI level-2 UV aerosol index product reports a value below 0.0, the pixel is not processed and a flag is raised. If the value is less than 1.0, a low UVAI flag is raised.
7. If the reported cloud fraction values from the TROPOMI FRESCO product for the pixel is beyond 0.6, the pixel is not processed and a flag is raised.
8. If the VIIRS average cirrus reflectance for the pixel is beyond 0.4, the pixel is not processed and a flag is raised. If it is beyond 0.01, a warning for possible cirrus clouds is indicated.
9. If the difference between the scene albedo (calculated using a look up table) from the Level-2 UVAI product and the surface albedo from the Tilstra et al. (2017) database at 380 nm is beyond 0.4, the pixel is removed from the processing pool and a flag is raised for possible cloud contamination. If this is value is beyond 0.2, a warning flag is raised.
10. The nominal TROPOMI pixels also contain radiances at a sub-pixel level, which are called small pixel radiances. If the standard deviation of the small pixel radiances is larger than 1×10^7 , the scene is deemed to be non-homogeneous (possibly containing clouds) and it is removed from the processing pool.

These relevant flags are reported in Table 1 and are available in the level-2 data products; the values for each of these flags can be accessed with bitwise and operations for each pixel with the value of each processing quality flag. For cloud filtering, the cloud_warning flag is the preferred flag for removing possibly cloudy pixels. This flag is a combination of FRESCO cloud fraction retrievals, VIIRS cirrus reflectance retrievals and the difference between the surface albedo and the scene albedo at 380 nm. An example of applying the cloud_warning flags to filter out possibly cloudy pixels is provided in Figure 1.

2.2 CALIOP weighted extinction height

The Cloud-Aerosol LIDAR with Orthogonal Polarisation (CALIOP) instrument is a part of the payload for the Cloud-Aerosol LIDAR and Infrared Pathfinder Satellite Observation (CALIPSO) mission (Winker et al., 2009), which orbits the Earth in a sun-synchronous orbit. The CALIOP instrument has three backscatter receiver channels, two channels for the orthogonal measurement of received backscatter signal at 532 nm and one channel for backscatter at 1064 nm. LIDAR profiles from the CALIPSO mission are a good source of data for validating retrieved ALHs from TROPOMI, because of their ability to map the vertical structure of the atmosphere. The data from the CALIOP instrument relevant for validating TROPOMI ALH are the level-1 backscatter profiles and the level-2 aerosol extinction profiles, which are used at the same time.

Table 1. Processing Quality Flags relevant for diagnosing SSP ALH product quality. The descriptions are derived from the SSP IOOD (Input Output Data Definition).

name	value	description
CONVERGED PIXELS		
success	0	successful retrieval; warnings still possible.
sun_glint_warning	2048	pixel is in sun-glnt region
cloud_warning	32768	combination of different cloud detection methods
UVAI_warning	65536	UVAI is lower than 1.0
snow_ice_warning	16384	scene contains snow/ice
NON-CONVERGED or MISSING PIXELS		
convergence_error	19	optimal estimation did not converge
sza_range_error	7	Solar zenith $\geq 75^\circ$
max_iteration_convergence_error	21	no convergence; retrieval exceeds maximum iterations
aot_lower_boundary_error	22	no convergence; AOT ≤ 0.0 twice in succession
other_boundary_convergence_error	23	no convergence; state vector element crosses boundary conditions twice
solar_eclipse_filter	64	pixel not processed because of solar eclipse
cloud_filter	65	pixel skipped; FRESKO cloud fraction greater than 0.6
altitude_roughness_filter	67	pixel skipped; standard deviation of digital elevation model in pixel > 1000.0 m
snow_ice_filter	70	pixel skipped; pixel contains snow/ice
UVAI_filter	71	pixel skipped; UVAI < 0.0
cloud_fraction_fresco_filter	72	pixel skipped; cloud fraction > 0.6
cirrus_reflectance_viirs_filter	76	pixel skipped; VIIRS cirrus reflectance > 0.4

In this paper, the level-1 total backscatter profiles from the 532 nm channel are used as curtain plots to visualise the vertical structure of the atmosphere. Level-2 aerosol extinction profiles from the 532 nm channel are then used to compute an aerosol weighted extinction height ALH_{ext} , following the definition provided by Equation 1 in Koffi et al. (2012),

$$ALH_{ext} = \frac{\sum_{i=1}^n \beta_{ext,i} Z_i}{\sum_{i=1}^n \beta_{ext,i}}, \quad (2)$$

- 5 where Z_i is the height from sea level in the i^{th} LIDAR vertical level i (in km), and $\beta_{ext,i}$ is the aerosol extinction coefficient (in km^{-1}) at the same level. The Level-2 aerosol extinction profile product from CALIOP only includes atmospheric levels where aerosols are detected. In the case when aerosols are present over clouds, ALH_{ext} will be situated to the center of the aerosol layer, with any possibly undetected aerosol layers below the cloud layer not included in the calculations due to attenuation

of the signal beyond the cloud layer. This is an important detail as the TROPOMI ALH algorithm cannot separate cloud and aerosol signals from the measured radiances, and cloud contamination will affect the retrieved product. In this paper, the CALIOP 532 nm channel observations are chosen for analysis as the conclusions from the analysis of the results do not change when the 1064 nm channel observations are used instead. Appendix A explains the collocation technique used in this paper. The CALIOP aerosol product might be cloud contaminated as well, but this is difficult to ascertain. Plotting ALH_{ext} over curtain plots of level-1 total backscatter profiles can be used to visually discern possibly cloud-contaminated CALIOP level-2 aerosol product.

3 Results

3.1 Comparison of TROPOMI ALH and CALIOP ALH_{ext}

TROPOMI-CALIOP collocations between 1st of May 2018 to the 28th of February 2019 are selected. Two sets of overall comparisons are done between CALIOP ALH_{ext} and TROPOMI ALH, one with all collocations (Figure 2a) regardless of cloud filtering and the other with a smaller subset of the dataset constrained by the cloud_warning flag from Table 1 (Figure 2b). The contrast between retrievals over land and ocean is apparent in Figure 3 (clouds flagged) — a majority of the negative differences with values lower than -2 km occur over land.

From Figure 2a, what is immediately clear is that the CALIOP ALH_{ext} are higher than the TROPOMI ALH. With an average difference of -2.25 km, median difference of -1.62 km and a standard deviation of 3.83 km, the retrieved ALH from TROPOMI over land is reported to be systematically closer to the surface than CALIOP ALH_{ext} than in comparison with retrievals over the ocean, which has a mean difference of -0.41 km, a median difference of -0.29 km and a very high standard deviation of 6.86 km. There are several cases over the ocean where TROPOMI ALH is significantly higher than the CALIOP ALH_{ext} , which could be due to cloud contamination. The comparison of the cloud-screened retrievals (Figure 2b) reveals that the retrieved ALH from TROPOMI over the ocean differs from CALIOP ALH_{ext} by -1.03 km on average, a median difference of -0.76 km and a standard deviation of 1.97 km. More than 50% of the TROPOMI ALH retrievals over the ocean have an absolute difference with ALH_{ext} less than 1.0 km. Retrievals over land are have a larger difference, with -2.41 km on average and a median of -1.75 km. The results are very skewed over land, with very large negative values dictating the average — this is indicated by the very large standard deviation of 3.56 km. 50% of the selected collocations over land have an absolute difference with ALH_{ext} less than approximately 1.8 km.

The distribution of the differences between TROPOMI ALH and CALIOP ALH_{ext} as a function of the retrieved UVAI (Figure 4a) shows that for most cases, the UVAI is below 2.0. The spread of the differences in this UVAI regime is large, which reduces as the UVAI increases. The differences seem to be less often positive as the UVAI increases; if compared with the behaviour observed between Figure 2a and Figure 2b where a majority of the positive differences vanish once the data is cloud screened, such a behaviour could be related to clouds. The distribution of the differences as a function of retrieved AOT in Figure 4b show that the majority of the collocations have AOT values between 0 and 2. Finally, the distribution of these differences as a function of the GOME-2 LER values used for the retrievals for cases over land show that the retrievals tend to

have a lower difference as the LER value increases — this could be a consequence of the fact that so few retrievals converge in high LER regimes that, unless the aerosol layer has a significant contribution to the measured top of atmosphere radiance in comparison to the surface, the retrievals tend to fail.

Retrieved ALH over land (if successful) can be closer to the surface than where the aerosol layer actually is situated vertically. The TROPOMI ALH product, unlike the CALIOP ALH_{ext} which only considers aerosol signatures in the recorded backscatter profile, is also influenced by the presence of undetected clouds. These are some of the several possible sources of departures between the observations of CALIOP and TROPOMI over the same scene. In the next section, the comparison between TROPOMI ALH and CALIOP ALH_{ext} is extended for a few selected scenes.

3.2 Analysis of selected cases

10 3.2.1 Selected cases

The analysis presented in the previous section alone is insufficient to fully quantify the quality of the retrieved TROPOMI ALHs, due to the manner in which clouds are handled by both aerosol heights; TROPOMI pixels are affected by the presence of undetected clouds whereas CALIOP aerosol extinction profiles do not consider clouds. Another significant source of departure between TROPOMI and CALIOP are their different sensing principles. Making conclusions on the quality of the current TROPOMI ALH product requires case-by-case studies of selected scenes. In line with this, four cases are selected to represent a very good mix of scenes containing elevated aerosol layers as well as aerosol layers close to the surface, high and low UV aerosol index, clear and cloudy scenes, clouds over and below aerosol layers, multiple aerosol layers, and retrievals over land and the ocean.

The cases selected are Saharan desert dust and biomass burning events, three off the west coast of Sahara (desert dust) in June 2018 and one off the South Saharan coast (biomass burning) in December 2018. All four cases have very good collocations between TROPOMI and CALIOP, with the CALIOP ground track over the aerosol plumes (plotted with a yellow line over the VIIRS images in Figure 5 (1st column). The operational ALH level-2 algorithm operates on pixels falling within the sun-glint regime, however they are excluded from the analyses presented in this paper. The retrieved UV aerosol index (UVAI) from the operational level-2 UVAI product gives an idea about the shape of the aerosol plumes in all these cases (Figure 5 (2nd column)). The UVAI is influenced by many factors including the ALH, with lower UVAI values for aerosol layers closer to the surface (discussed further in Appendix B). Cases a and b contain several pixels with UVAI values greater than 3.0, whereas a majority of the TROPOMI pixels in cases c and d have TROPOMI UVAI values between 0.0 and 2.0. A significant majority of successful retrievals in these selected scenes are over a dark surface, owing to the bright surface albedo of the Saharan desert. The reader is point to Griffin et al. (2019) for comparison of the TROPOMI ALH retrievals over land for biomass burning aerosol plumes with the same from several other instruments including CALIOP.

It is important to note that spaceborne LIDARs, while having the advantage of being able to map more than one vertical layer in the atmosphere, suffer from attenuation of the signal in the presence of strongly backscattering components such as clouds or aerosols with a large optical depth. In the presence of a primary strongly backscattering aerosol layer, the attenuation of the

signal may lead to undetected secondary aerosol layers beneath the primary layer. These layers, not apparent in the CALIOP curtain plots of the measured attenuated backscatter profiles, may be detected by the level 2 aerosol extinction profile product from the CALIOP mission, using the formula described in Equation 2. Some of these discussed situations are observed in the CALIOP curtain plots of the selected cases in Figure 6, especially for cases a and b, where the attenuated signal does not detect possibly lower aerosol or cloud layers, and in case d where the attenuation of the signal due to a thick aerosol plume can hide the surface from the received backscatter signal. TROPOMI, on the other hand, will tend to report an ALH between these two layers as it will be influenced by photons scattered back from both layers.

3.2.2 Analysis

The retrieved TROPOMI ALH in Figure 5 (4th column) represent successful retrievals for each of the selected cases. Beyond the sun glint warning, the cloud_warning flag in Table 1 is applied to remove possibly cloud contaminated data. The retrieved aerosol optical thickness (AOT), which is a part of the state vector, for each of the scenes are plotted over the VIIRS image of the scene in Figure 5 (3rd column). The retrieved AOT (τ_{aer}) can act as a diagnostic tool to indicate the influence of the surface (over bright surfaces) or the presence of undetected clouds (both over bright and dark surfaces) — in these cases, the retrieved AOT of the scene can be uncharacteristically high with values much greater than 3.0. All retrieved TROPOMI AOT values beyond 5.0 are discarded as the neural network forward models are trained with AOT values less than or equal to 5.0.

A visual inspection of Figure 5 shows that the retrieved UVAI, AOT and ALH need not be spatially correlated, as they are separate properties of the observed aerosol plumes — for instance, if the retrieved UVAI and AOT are low (case c), the retrieved ALH need not necessarily be low. An inspection the retrieved AOT for cases c (between latitudes 10° and 15° and longitude -20°) and d reveal square structures, both over the ocean and land. These square shaped spatial artefacts are the surface albedo grids derived from the database provided by Tilstra et al. (2017), which is the current source for surface reflectance in the ALH retrieval algorithm. In case c, the retrieved AOT contains surface information influenced by the assumed albedo in the database. These spatial features are not as apparent in cases a and b (Figure 5, 1st and 2nd rows) as a majority of the signal in the measured top of atmosphere radiances come from aerosols and the minority from the surface. Another major observation is the lack of retrievals over the desert. This is within expectation, as measurements of the top of atmosphere radiances over a cloud-free desert scene tend to contain more photons scattered back from the surface than the aerosol layer. As a result, retrievals over bright scenes are sensitive to the assumed errors in the surface albedo, thereby reducing sensitivity to the assumed ALH (Sanders et al. (2015), Section 2, Figure 2).

While scenes not contaminated with clouds show a smooth spatial distribution of the retrieved ALH, the presence of clouds may or may not add spatial variability in the ALH product. For instance, the the presence of low clouds are clear in case b (Figure 5b) beyond latitude 21.0°, but the retrieved ALH is spatially homogeneous with values less than 1.0 km. For each of the selected cases, colocated CALIOP profiles in Figure 6 give additional information about the scene. These TROPOMI-CALIOP colocations are done via the method discussed in Appendix A. The CALIOP curtain plot for case b reveals the influence of low clouds as well as high clouds on the cloud-screened ALH. An example of cloud-contaminated heterogeneous vertical distribution of TROPOMI ALH in Figure 6a can be observed between latitudes 9.5° and 11.0°. The cloud filtering following

the cloud_warning flag in Table 1 does not detect these low clouds (for instance above latitude 21.5°, see Figure 6 a, b). These are manually for comparison further on.

From Figure 2b, TROPOMI retrievals of ALH over bright surfaces are expected to differ from CALIOP ALH_{ext}, wherein the TROPOMI ALH product may report ALH estimates closer to the surface than CALIOP will. This is observed in case d (Figure 5, bottom row), wherein the CALIOP curtain plot for (Figure 6d) indicates that the plume is close to the surface, with a maximum height less than 3 km; TROPOMI ALH for biomass burning aerosol plume that extends from land to the ocean is slightly closer to the surface in the case of land when compared to CALIOP ALH_{ext}, whereas over the ocean both height estimates more or less are in agreement.

For cases a and b, retrieved TROPOMI ALH does not seem to coincide with large values of the received backscatter signal in the level-1 data, whereas it does for case c, and to a certain extent for case d (over land it tends to be closer to the surface). Parts of the CALIOP curtain plots for cases a, b and c suggest the existence of a possible second layer beneath the layer that is visually obvious, or that the desert dust layer extends deeper to the surface and the CALIOP signal is simply too attenuated to detect it.

A direct comparison of the CALIOP ALH_{ext} and TROPOMI ALH for these four selected cases are presented in Figure 7. For this comparison, every cloud-filtered and sun-glint-filtered TROPOMI pixel with ALH information colocated to a specific CALIOP level-2 aerosol extinction profile in Figure 6 is averaged and a standard deviation is also computed. These averaged TROPOMI ALH are then compared to the CALIOP ALH_{ext}, and show that TROPOMI ALH differ from CALIOP ALH_{ext} by 0.53 km, with a pearson correlation coefficient of 0.64 and a slope of 1.0; CALIOP ALH_{ext} are systematically higher than TROPOMI ALH (indicated by a y-intercept of the fit at 0.53 km). The CALIOP ALH_{ext} is also higher than TROPOMI ALH almost consistently in most cases. This could possibly be due to CALIOP possibly underestimating the aerosol layer thickness due to strong attenuation of the LIDAR signal at the top of the aerosol layer (Rajapakshe et al., 2017), whereas TROPOMI ALH product does not suffer from such attenuation.

4 Discussion and conclusion

This paper discusses the quality of the soon to be released TROPOMI ALH product by comparing it with CALIOP data of colocated measurements of scenes containing aerosols between the two instruments. In order to do so, CALIOP weighted extinction heights from the 532 nm channel were calculated following Equation 2, and then directly compared to TROPOMI ALH. Further on, four individual cases of Saharan desert dust and biomass burning aerosol events in 2018 were selected for a deeper analysis of the product's quality.

From the analysis presented in this paper, TROPOMI's neural network ALH retrieval algorithm retrieves ALH values that compare well with CALIOP weighted extinction heights in cloud-screened cases following the cloud screening strategy using the TROPOMI ALH level-2 processing quality flags discussed in Table 1. For more than 1 million collocations between CALIOP and TROPOMI over the ocean, the TROPOMI ALH differs from CALIOP ALH_{ext} by approximately -1 km on average and -0.76 km median, with the TROPOMI ALH values being lower than the CALIOP ALH_{ext}. Over land, the same values

are -2.41 km on average and -1.75 km as the median. To get a better understanding of the differences between TROPOMI and CALIOP retrieved aerosol heights, this paper compared the ALH for selected cases among the more 1 million collocations that were better understood. The four selected scenes were chosen around the West Saharan region, where a majority of the TROPOMI-CALIOP collocations were found. For the selected cases, largely over the ocean within a portion of the data over
5 land, the averaged retrieved ALH from TROPOMI differed from CALIOP ALH_{ext} by 0.53 km, with CALIOP ALH_{ext} being higher than TROPOMI ALH. These numbers are indicative that TROPOMI ALH performs well, especially considering the many simplifications made by the retrieval algorithm in order to optimise on the computational speed; future improvements to the forward model may only improve the product further on.

There is a clear distinction between TROPOMI ALH retrievals over land and the ocean as photons scattering back from
10 bright surfaces tend to influence ALH estimates closer towards the surface than an elevated aerosol layer. Retrieved ALH over land, if successful, can be closer to the surface if measured signal in the top of atmosphere contains more photons scattered back from the deepest atmospheric layer which is the surface, in comparison to elevated aerosol layers which are higher up in the atmosphere. This, however can change depending on the amount of aerosol information available in the spectrum compared to same from the surface. Any attempt in retrieving ALH over the desert generally fail, with very few exceptions. There are
15 several challenges, that will need further development.

The TROPOMI level-2 UVAI product is currently an ingredient in selecting pixels containing aerosols for retrieving ALH. While this choice works quite well for cloud free scenarios, it does not do a great job when a scene that contains both aerosols and clouds. These cloudy scenes do not seem to be detected by the current cloud filtering schematic in the level-2 algorithm, and will require a significant update in deciding whether a pixel is cloudy or not. For cases scenes with a low aerosol load,
20 square shaped artefacts resulting from a surface albedo database with a resolution significantly lower than TROPOMI exist. Currently, the GOME-2 surface LER product derived from Tilstra et al. (2017) is used operationally, and will eventually need to be updated with a higher resolution version possibly derived from TROPOMI itself. To that extent, owing to the boost in the computational speed of the radiative transfer calculations, the algorithm can now incorporate more complex aerosol property and profile parameterizations. Such a step will benefit the TROPOMI ALH retrieval accuracy significantly.

25 Finally, space based LIDAR (such as the CALIOP instrument on board the CALIPSO mission) is a very good tool to retrieve aerosol vertical information to validate the TROPOMI ALH product. While the CALIOP level-1 backscatter profiles may be attenuated in cases of very strong signals from the top of the aerosol layer, the weighted extinction heights in conjunction with the backscatter profiles are sufficient for validation activities. These CALIOP profiles will be very important in assessing the impact of future development activities of the TROPOMI ALH product.

30 **Appendix A: Colocation**

The colocation between TROPOMI and CALIOP ground pixels is done in the following manner. First, the geographic coordinates of CALIOP level 1 backscatter profiles and level 2 aerosol extinction profiles are converted into the Cartesian coordinate system. These CALIOP coordinates are fed into a k-dimensional tree, which is a fast algorithm developed by Maneewong-

vatana and Mount (1999) to quickly locate the nearest neighbour of a point (a TROPOMI ground pixel) to a k-dimensional tree of points (CALIOP ground pixels). The `scipy.spatial.KDtree` module (Maneewongvatana and Mount, 1999) in python3 is used to create the k-dimensional tree of the ground coordinates of CALIOP profiles (separate for level 1 and level 2 data). Second, all TROPOMI ground pixel coordinates are converted to Cartesian coordinates. For each of these TROPOMI pixels, the distance to the nearest CALIOP profile is queried using the `scipy.spatial.KDtree.query` function. This creates a list of TROPOMI pixels and their nearest CALIOP profile and a distance in meters. Finally, only colocations with a maximum distance of 100 km and a maximum time difference of 5 hours are selected. A map of all 2,474,042 colocations (in Figure 8) shows that most of the colocations are close to the continent of Africa. After filtering out all colocations in the TROPOMI sun-glint region, all retrieved AOTes greater than 5.0 (as the neural network is trained for all AOT less than 5.0), and filtering out ocean pixels with a surface albedo greater than 0.05 and land pixels with a surface albedo less than 0.1 and greater than 0.4, there are in total 731,347 TROPOMI pixels entirely over land and 1,742,695 pixels entirely over water (see Figure 2a). After cloud screening using the `cloud_warning` flag in Table 1, a total of 546,445 pixels over land and 1,036,550 pixels over the ocean remain (see Figure 2b).

Appendix B: UVAI Sensitivity to ALH

It is well-documented that the UVAI depends on ALH (Herman et al., 1997; Torres et al., 1998; de Graaf, 2005; Sun et al., 2018). Absorbing aerosols mainly interact with molecular scattered radiation beneath the aerosol layer. The higher the layer, the more Rayleigh scattering underneath is shielded, leading to a high UVAI value (Figure 9a). This altitude dependence increases with aerosol single scattering albedo) and aerosol loading (i.e. AOT), whereas it becomes weaker over brighter surfaces where the importance of molecular scattering reduces significantly (Figure 9b). On the other hand, little altitude dependence is found for non-absorbing aerosols (i.e. SSA = 0.99). The conclusions from this synthetic experiment are replicate with real TROPOMI data in a separate manuscript, where for retrieved ALH for pixels with a UVAI greater than 1 for measurements from TROPOMI showed an increase in the correlation as well as the slope between ALH and UVAI for an increase in MODIS AOT values for the same scenes. This manuscript is currently submitted to Atmospheric Chemistry and Physics and awaits review.

Competing interests. The author declares no conflict of interests in the work expressed in this publication.

Acknowledgements. This publication contains modified Copernicus Sentinel data. This research is partly funded by the European Space Agency (ESA) within the EU Copernicus programme. We acknowledge the use of VIIRS imagery from the NASA Worldview application (<https://worldview.earthdata.nasa.gov/>), part of the NASA Earth Observing System Data and Information System (EOSDIS).

References

- Barkley, A. E., Prospero, J. M., Mahowald, N., Hamilton, D. S., Popendorf, K. J., Oehlert, A. M., Pourmand, A., Gatineau, A., Panechou-Pulcherie, K., Blackwelder, P., and Gaston, C. J.: African biomass burning is a substantial source of phosphorus deposition to the Amazon, Tropical Atlantic Ocean, and Southern Ocean, *Proceedings of the National Academy of Sciences*, p. 201906091, <https://doi.org/10.1073/pnas.1906091116>, <https://www.pnas.org/content/early/2019/07/23/1906091116>, 2019.
- 5 Chimot, J., Veefkind, J. P., Vlemmix, T., de Haan, J. F., Amiridis, V., Proestakis, E., Marinou, E., and Levelt, P. F.: An exploratory study on the aerosol height retrieval from OMI measurements of the 477 nm O₂O₂ spectral band using a neural network approach, *Atmos. Meas. Tech.*, 10, 783–809, <https://doi.org/10.5194/amt-10-783-2017>, <https://www.atmos-meas-tech.net/10/783/2017/>, 2017.
- Chimot, J., Veefkind, J. P., Vlemmix, T., and Levelt, P. F.: Spatial distribution analysis of the OMI aerosol layer height: a pixel-by-pixel comparison to CALIOP observations, *Atmos. Meas. Tech.*, 11, 2257–2277, <https://doi.org/10.5194/amt-11-2257-2018>, <https://www.atmos-meas-tech.net/11/2257/2018/>, 2018.
- 10 Choi, W., Lee, H., Kim, J., Ryu, J. Y., Park, S. S., Park, J., and Kang, H.: Effects of spatiotemporal O₄ column densities and temperature-dependent O₄ absorption cross-section on an aerosol effective height retrieval algorithm using the O₄ air mass factor from the ozone monitoring instrument, *Remote Sensing of Environment*, 229, 223–233, <https://doi.org/10.1016/j.rse.2019.05.001>, <https://yonsei.pure.elsevier.com/en/publications/effects-of-spatiotemporal-osub4sub-column-densities-and-temperatu>, 2019.
- 15 Davis, A. B., Kalashnikova, O. V., and Diner, D. J.: Aerosol Layer Height over Water from O₂ A-Band: Mono-Angle Hyperspectral and/or Bi-Spectral Multi-Angle Observations, <https://doi.org/10.20944/preprints201710.0055.v1>, 2017.
- de Graaf, M.: Absorbing Aerosol Index: Sensitivity analysis, application to GOME and comparison with TOMS, *Journal of Geophysical Research*, 110, <https://doi.org/10.1029/2004JD005178>, <http://doi.wiley.com/10.1029/2004JD005178>, 2005.
- 20 de Haan, J. F., Bosma, P. B., and Hovenier, J. W.: The adding method for multiple scattering calculations of polarized light, *Astronomy and Astrophysics*, 183, 1987.
- de Rooij, W. A. and van der Stap, C. C. A. H.: Expansion of Mie scattering matrices in generalized spherical functions, *Astronomy and Astrophysics*, 131, 237–248, <http://adsabs.harvard.edu/abs/1984A%26A...131..237D>, 1984.
- Dubovik, O., Holben, B., Eck, T. F., Smirnov, A., Kaufman, Y. J., King, M. D., Tanré, D., and Slutsker, I.: Variability of Absorption and Optical Properties of Key Aerosol Types Observed in Worldwide Locations, *Journal of the Atmospheric Sciences*, 59, 590–608, [https://doi.org/10.1175/1520-0469\(2002\)059<0590:VOAAOP>2.0.CO;2](https://doi.org/10.1175/1520-0469(2002)059<0590:VOAAOP>2.0.CO;2), <https://journals.ametsoc.org/doi/full/10.1175/1520-0469%282002%29059%3C0590%3AVOAAOP%3E2.0.CO%3B2>, 2002.
- 25 Griffin, D., Sioris, C., Chen, J., Dickson, N., Kovachik, A., Graaf, M. d., Nanda, S., Veefkind, P., Dammers, E., McLinden, C. A., Makar, P., and Akingunola, A.: The 2018 fire season in North America as seen by TROPOMI: aerosol layer height validation and evaluation of model-derived plume heights, *Atmospheric Measurement Techniques Discussions*, pp. 1–30, <https://doi.org/https://doi.org/10.5194/amt-2019-411>, <https://www.atmos-meas-tech-discuss.net/amt-2019-411/#discussion>, 2019.
- 30 Henyey, L. C. and Greenstein, J. L.: Diffuse radiation in the Galaxy, *The Astrophysical Journal*, 93, 70, <https://doi.org/10.1086/144246>, <http://adsabs.harvard.edu/doi/10.1086/144246>, 1941.
- Herman, J. R., Bhartia, P. K., Torres, O., Hsu, C., Sefstor, C., and Celarier, E.: Global distribution of UV-absorbing aerosols from Nimbus 7/TOMS data, *Journal of Geophysical Research: Atmospheres*, 102, 16 911–16 922, <https://doi.org/10.1029/96JD03680>, <http://doi.wiley.com/10.1029/96JD03680>, 1997.
- 35

- Holben, B. N., Eck, T. F., Slutsker, I., Tanré, D., Buis, J. P., Setzer, A., Vermote, E., Reagan, J. A., Kaufman, Y. J., Nakajima, T., Lavenu, F., Jankowiak, I., and Smirnov, A.: AERONET—A Federated Instrument Network and Data Archive for Aerosol Characterization, *Remote Sensing of Environment*, 66, 1–16, [https://doi.org/10.1016/S0034-4257\(98\)00031-5](https://doi.org/10.1016/S0034-4257(98)00031-5), <http://www.sciencedirect.com/science/article/pii/S0034425798000315>, 1998.
- 5 Ingmann, P., Veihelmann, B., Langen, J., Lamarre, D., Stark, H., and Courrèges-Lacoste, G. B.: Requirements for the GMES Atmosphere Service and ESA's implementation concept: Sentinels-4/-5 and -5p, *Remote Sensing of Environment*, 120, 58–69, <https://doi.org/10.1016/j.rse.2012.01.023>, <http://linkinghub.elsevier.com/retrieve/pii/S0034425712000673>, 2012.
- IPCC: Clouds and Aerosols, in: *Climate Change 2013 - The Physical Science Basis*, pp. 571–658, Cambridge University Press, Cambridge, <https://doi.org/10.1017/CBO9781107415324.016>, <http://ebooks.cambridge.org/ref/id/CBO9781107415324A024>, 2014.
- 10 Kim, J., Jeong, U., Ahn, M.-H., Kim, J. H., Park, R. J., Lee, H., Song, C. H., Choi, Y.-S., Lee, K.-H., Yoo, J.-M., Jeong, M.-J., Park, S. K., Lee, K.-M., Song, C.-K., Kim, S.-W., Kim, Y. J., Kim, S.-W., Kim, M., Go, S., Liu, X., Chance, K., Chan Miller, C., Al-Saadi, J., Veihelmann, B., Bhartia, P. K., Torres, O., Abad, G. G., Haffner, D. P., Ko, D. H., Lee, S. H., Woo, J.-H., Chong, H., Park, S. S., Nicks, D., Choi, W. J., Moon, K.-J., Cho, A., Yoon, J., Kim, S.-k., Hong, H., Lee, K., Lee, H., Lee, S., Choi, M., Veefkind, P., Levelt, P. F., Edwards, D. P., Kang, M., Eo, M., Bak, J., Baek, K., Kwon, H.-A., Yang, J., Park, J., Han, K. M., Kim, B.-R., Shin, H.-W., Choi, H.,
- 15 Lee, E., Chong, J., Cha, Y., Koo, J.-H., Irie, H., Hayashida, S., Kasai, Y., Kanaya, Y., Liu, C., Lin, J., Crawford, J. H., Carmichael, G. R., Newchurch, M. J., Lefer, B. L., Herman, J. R., Swap, R. J., Lau, A. K. H., Kurosu, T. P., Jaross, G., Ahlers, B., Dobber, M., McElroy, C. T., and Choi, Y.: New Era of Air Quality Monitoring from Space: Geostationary Environment Monitoring Spectrometer (GEMS), *Bulletin of the American Meteorological Society*, 101, E1–E22, <https://doi.org/10.1175/BAMS-D-18-0013.1>, <https://journals.ametsoc.org/doi/full/10.1175/BAMS-D-18-0013.1>, 2019.
- 20 Kim, M., Kim, J., Torres, O., Ahn, C., Kim, W., Jeong, U., Go, S., Liu, X., Moon, K. J., and Kim, D.-R.: Optimal Estimation-Based Algorithm to Retrieve Aerosol Optical Properties for GEMS Measurements over Asia, *Remote Sensing*, 10, 162, <https://doi.org/10.3390/rs10020162>, <https://www.mdpi.com/2072-4292/10/2/162>, 2018.
- Koffi, B., Schulz, M., Bréon, F.-M., Griesfeller, J., Winker, D., Balkanski, Y., Bauer, S., Berntsen, T., Chin, M., Collins, W. D., Dentener, F., Diehl, T., Easter, R., Ghan, S., Ginoux, P., Gong, S., Horowitz, L. W., Iversen, T., Kirkevåg, A., Koch, D., Krol, M., Myhre, G.,
- 25 Stier, P., and Takemura, T.: Application of the CALIOP layer product to evaluate the vertical distribution of aerosols estimated by global models: AeroCom phase I results, *Journal of Geophysical Research: Atmospheres*, 117, <https://doi.org/10.1029/2011JD016858>, <https://agupubs.onlinelibrary.wiley.com/doi/abs/10.1029/2011JD016858>, 2012.
- Li, J., Carlson, B. E., and Laci, A. A.: A study on the temporal and spatial variability of absorbing aerosols using Total Ozone Mapping Spectrometer and Ozone Monitoring Instrument Aerosol Index data, *Journal of Geophysical Research: Atmospheres*, 114, <https://doi.org/10.1029/2008JD011278>, <https://agupubs.onlinelibrary.wiley.com/doi/abs/10.1029/2008JD011278>, 2009.
- Maneewongvatana, S. and Mount, D. M.: Analysis of approximate nearest neighbor searching with clustered point sets, *arXiv:cs/9901013*, <http://arxiv.org/abs/cs/9901013>, arXiv: cs/9901013, 1999.
- Nanda, S., de Graaf, M., Sneep, M., de Haan, J. F., Stammes, P., Sanders, A. F. J., Tuinder, O., Veefkind, J. P., and Levelt, P. F.: Error sources in the retrieval of aerosol information over bright surfaces from satellite measurements in the oxygen A band, *Atmos. Meas. Tech.*, 11, 161–175, <https://doi.org/10.5194/amt-11-161-2018>, <https://www.atmos-meas-tech.net/11/161/2018/>, 2018a.
- 30 Nanda, S., Veefkind, J. P., de Graaf, M., Sneep, M., Stammes, P., de Haan, J. F., Sanders, A. F. J., Apituley, A., Tuinder, O., and Levelt, P. F.: A weighted least squares approach to retrieve aerosol layer height over bright surfaces applied to GOME-2 measurements of the

- oxygen A band for forest fire cases over Europe, *Atmos. Meas. Tech.*, 11, 3263–3280, <https://doi.org/10.5194/amt-11-3263-2018>, <https://www.atmos-meas-tech.net/11/3263/2018/>, 2018b.
- Nanda, S., Graaf, M. d., Veefkind, J. P., Linden, M. t., Sneep, M., Haan, J. d., and Levelt, P. F.: A neural network radiative transfer model approach applied to TROPOMI's aerosol height algorithm, *Atmospheric Measurement Techniques Discussions*, pp. 1–24, <https://doi.org/https://doi.org/10.5194/amt-2019-143>, <https://www.atmos-meas-tech-discuss.net/amt-2019-143/>, 2019.
- 5 Nelson, D. L., Garay, M. J., Kahn, R. A., and Dunst, B. A.: Stereoscopic Height and Wind Retrievals for Aerosol Plumes with the MISR INteractive eXplorer (MINX), *Remote Sensing*, 5, 4593–4628, <https://doi.org/10.3390/rs5094593>, <https://www.mdpi.com/2072-4292/5/9/4593>, 2013.
- Park, S. S., Kim, J., Lee, H., Torres, O., Lee, K.-M., and Lee, S. D.: Utilization of O₄ slant column density to derive aerosol layer height from a space-borne UV–visible hyperspectral sensor: sensitivity and case study, *Atmospheric Chemistry and Physics*, 16, 1987–2006, <https://doi.org/https://doi.org/10.5194/acp-16-1987-2016>, <https://www.atmos-chem-phys.net/16/1987/2016/>, 2016.
- 10 Rajapakshe, C., Zhang, Z., Yorks, J. E., Yu, H., Tan, Q., Meyer, K., Platnick, S., and Winker, D. M.: Seasonally transported aerosol layers over southeast Atlantic are closer to underlying clouds than previously reported, *Geophysical Research Letters*, 44, 5818–5825, <https://doi.org/10.1002/2017GL073559>, <https://agupubs.onlinelibrary.wiley.com/doi/abs/10.1002/2017GL073559>, 2017.
- 15 Rodgers, C. D.: *Inverse methods for atmospheric sounding: theory and practice*, vol. 2, World Scientific, 2000.
- Sanders, A. F. J. and de Haan, J. F.: TROPOMI ATBD of the Aerosol Layer Height product, http://www.tropomi.eu/sites/default/files/files/S5P-KNMI-L2-0006-RP-TROPOMI_ATBD_Aerosol_Height-v1p0p0-20160129.pdf, 2016.
- Sanders, A. F. J., de Haan, J. F., Sneep, M., Apituley, A., Stammes, P., Vieitez, M. O., Tilstra, L. G., Tuinder, O. N. E., Koning, C. E., and Veefkind, J. P.: Evaluation of the operational Aerosol Layer Height retrieval algorithm for Sentinel-5 Precursor: application to Oxygen A band observations from GOME-2A, *Atmospheric Measurement Techniques*, 8, 4947–4977, <https://doi.org/10.5194/amt-8-4947-2015>, <http://www.atmos-meas-tech.net/8/4947/2015/>, 2015.
- 20 Sun, J., Veefkind, J. P., Velthoven, P. v., and Levelt, P. F.: Quantifying the single-scattering albedo for the January 2017 Chile wildfires from simulations of the OMI absorbing aerosol index, *Atmospheric Measurement Techniques*, 11, 5261–5277, <https://doi.org/https://doi.org/10.5194/amt-11-5261-2018>, <https://www.atmos-meas-tech.net/11/5261/2018/amt-11-5261-2018.html>, 2018.
- 25 Tilstra, L. G., Tuinder, O. N. E., Wang, P., and Stammes, P.: Surface reflectivity climatologies from UV to NIR determined from Earth observations by GOME-2 and SCIAMACHY: GOME-2 and SCIAMACHY surface reflectivity climatologies, *Journal of Geophysical Research: Atmospheres*, <https://doi.org/10.1002/2016JD025940>, <http://doi.wiley.com/10.1002/2016JD025940>, 2017.
- Torres, O., Bhartia, P. K., Herman, J. R., Ahmad, Z., and Gleason, J.: Derivation of aerosol properties from satellite measurements of backscattered ultraviolet radiation: Theoretical basis, *Journal of Geophysical Research: Atmospheres*, 103, 17 099–17 110, <https://doi.org/10.1029/98JD00900>, <https://agupubs.onlinelibrary.wiley.com/doi/abs/10.1029/98JD00900>, 1998.
- Twomey, S.: Pollution and the planetary albedo, *Atmospheric Environment (1967)*, 8, 1251–1256, [https://doi.org/10.1016/0004-6981\(74\)90004-3](https://doi.org/10.1016/0004-6981(74)90004-3), <http://www.sciencedirect.com/science/article/pii/0004698174900043>, 1974.
- Vasilkov, A., Joiner, J., and Spurr, R.: Note on rotational-Raman scattering in the O₂ A- and B-bands, *Atmospheric Measurement Techniques*, 6, 981–990, <https://doi.org/https://doi.org/10.5194/amt-6-981-2013>, <https://www.atmos-meas-tech.net/6/981/2013/>, 2013.
- 35 Veefkind, J. P., Aben, I., McMullan, K., Förster, H., de Vries, J., Otter, G., Claas, J., Eskes, H. J., de Haan, J. F., Kleipool, Q., van Weele, M., Hasekamp, O., Hoogeveen, R., Landgraf, J., Snel, R., Tol, P., Ingmann, P., Voors, R., Kruizinga, B., Vink, R., Visser, H., and Levelt, P. F.: TROPOMI on the ESA Sentinel-5 Precursor: A GMES mission for global observations of the atmospheric composition for climate,

- air quality and ozone layer applications, *Remote Sensing of Environment*, 120, 70–83, <https://doi.org/10.1016/j.rse.2011.09.027>, <http://www.sciencedirect.com/science/article/pii/S0034425712000661>, 2012.
- Wagner, T., Beirle, S., Deutschmann, T., and Penning de Vries, M.: A sensitivity analysis of Ring effect to aerosol properties and comparison to satellite observations, *Atmospheric Measurement Techniques*, 3, 1723–1751, <https://doi.org/https://doi.org/10.5194/amt-3-1723-2010>,
5 <https://www.atmos-meas-tech.net/3/1723/2010/>, 2010.
- Wang, P., Stammes, P., van der A, R., Pinardi, G., and van Roozendael, M.: FRESCO+: an improved O2 A-band cloud retrieval algorithm for tropospheric trace gas retrievals, *Atmos. Chem. Phys.*, 8, 6565–6576, <https://doi.org/10.5194/acp-8-6565-2008>, <https://www.atmos-chem-phys.net/8/6565/2008/>, 2008.
- Winker, D. M., Vaughan, M. A., Omar, A., Hu, Y., Powell, K. A., Liu, Z., Hunt, W. H., and Young, S. A.: Overview of the
10 CALIPSO Mission and CALIOP Data Processing Algorithms, *Journal of Atmospheric and Oceanic Technology*, 26, 2310–2323, <https://doi.org/10.1175/2009JTECHA1281.1>, <https://journals.ametsoc.org/doi/full/10.1175/2009JTECHA1281.1>, 2009.
- Xu, X., Wang, J., Wang, Y., Zeng, J., Torres, O., Yang, Y., Marshak, A., Reid, J., and Miller, S.: Passive remote sensing of altitude and optical depth of dust plumes using the oxygen A and B bands: First results from EPIC/DSCOVER at Lagrange-1 point, *Geophysical Research Letters*, 44, 2017GL073939, <https://doi.org/10.1002/2017GL073939>, <http://onlinelibrary.wiley.com/doi/10.1002/2017GL073939/abstract>,
15 2017.
- Xu, X., Wang, J., Wang, Y., Zeng, J., Torres, O., Reid, J. S., Miller, S. D., Martins, J. V., and Remer, L. A.: Detecting layer height of smoke aerosols over vegetated land and water surfaces via oxygen absorption bands: hourly results from EPIC/DSCOVER in deep space, *Atmospheric Measurement Techniques*, 12, 3269–3288, <https://doi.org/https://doi.org/10.5194/amt-12-3269-2019>, <https://www.atmos-meas-tech.net/12/3269/2019/>, 2019.
- 20 Yu, H., Chin, M., Yuan, T., Bian, H., Remer, L. A., Prospero, J. M., Omar, A., Winker, D., Yang, Y., Zhang, Y., Zhang, Z., and Zhao, C.: The fertilizing role of African dust in the Amazon rainforest: A first multiyear assessment based on data from Cloud-Aerosol Lidar and Infrared Pathfinder Satellite Observations, *Geophysical Research Letters*, 42, 1984–1991, <https://doi.org/10.1002/2015GL063040>, <https://agupubs.onlinelibrary.wiley.com/doi/abs/10.1002/2015GL063040>, 2015.
- Zoogman, P., Liu, X., Suleiman, R. M., Pennington, W. F., Flittner, D. E., Al-Saadi, J. A., Hilton, B. B., Nicks, D. K., Newchurch, M. J.,
25 Carr, J. L., Janz, S. J., Andraschko, M. R., Arola, A., Baker, B. D., Canova, B. P., Chan Miller, C., Cohen, R. C., Davis, J. E., Dussault, M. E., Edwards, D. P., Fishman, J., Ghulam, A., González Abad, G., Grutter, M., Herman, J. R., Houck, J., Jacob, D. J., Joiner, J., Kerridge, B. J., Kim, J., Krotkov, N. A., Lamsal, L., Li, C., Lindfors, A., Martin, R. V., McElroy, C. T., McLinden, C., Natraj, V., Neil, D. O., Nowlan, C. R., OSullivan, E. J., Palmer, P. I., Pierce, R. B., Pippin, M. R., Saiz-Lopez, A., Spurr, R. J. D., Szykman, J. J., Torres, O., Veefkind, J. P., Veihelmann, B., Wang, H., Wang, J., and Chance, K.: Tropospheric emissions: Monitoring of pollution
30 (TEMPO), *Journal of Quantitative Spectroscopy and Radiative Transfer*, 186, 17–39, <https://doi.org/10.1016/j.jqsrt.2016.05.008>, <http://www.sciencedirect.com/science/article/pii/S0022407316300863>, 2017.

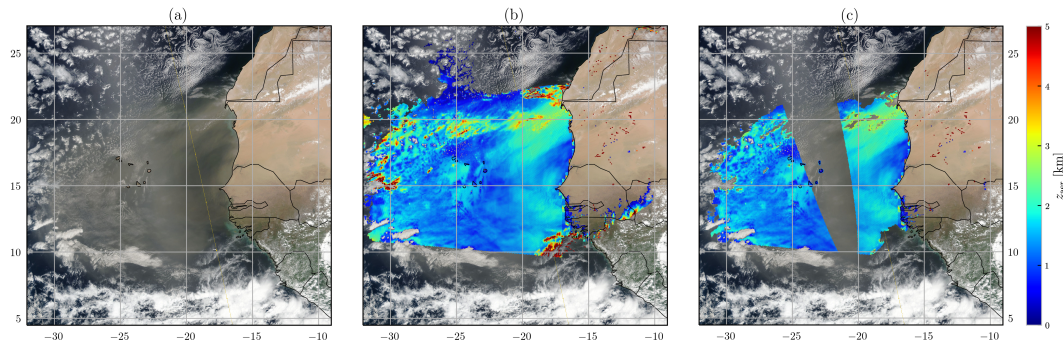


Figure 1. (a) A VIIRS corrected reflectance image over the West African coast on the 8th of June, 2018. (b) All successful TROPOMI retrievals within a certain bounding box. (c) Same as (b) but with all pixels that possibly fall within the sun glint region or are cloud contaminated are removed (using `cloud_warning` flag and `sun_glint_warning` from Table 1).

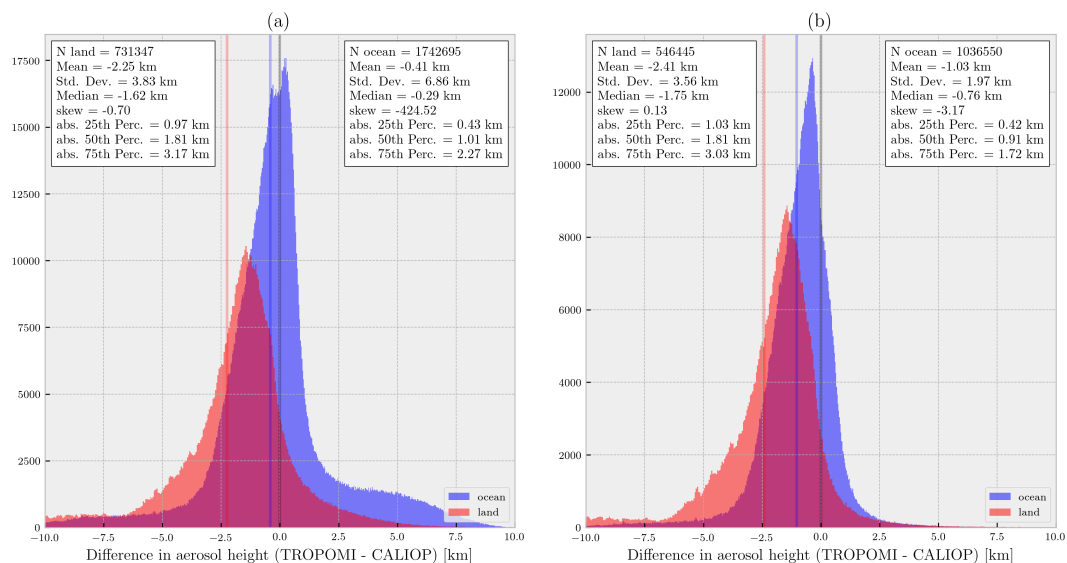


Figure 2. Histogram of differences between CALIOP ALH_{ext} (Equation 2) and TROPOMI ALH from colocated data between May 1, 2018 and February 28, 2019. Blue histogram represents TROPOMI pixels over the ocean whereas the red histogram is for TROPOMI pixels over land. The blue line represents the mean difference between TROPOMI ALH and CALIOP ALH_{ext} for TROPOMI pixels over the ocean, whereas the red line represents the same for TROPOMI pixels over land. The black line at 0.0 km difference on the x-axis is plotted to aid the reader in their interpretation of this figure. (a) All collocations except TROPOMI pixels falling in the sun glint region. TROPOMI pixels with retrieved AOT greater than 5.0 are discarded. For pixels over land, if the GOME-2 surface albedo is less than 0.1 or greater than 0.4, they are discarded. Similarly, over the ocean all TROPOMI pixels that have a GOME-2 surface albedo greater than 0.05 are discarded. (b) Same, except only TROPOMI ALH retrievals that are cloud-screened using `cloud_warning` flag from Table 1 are included.

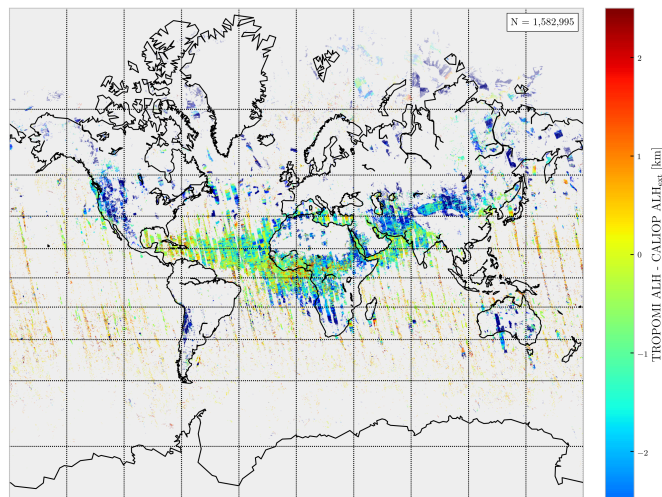


Figure 3. A map of cloud filtered and sun glint filtered differences between colocated TROPOMI ALH and CALIOP ALH_{ext} considered for Figure 2b.

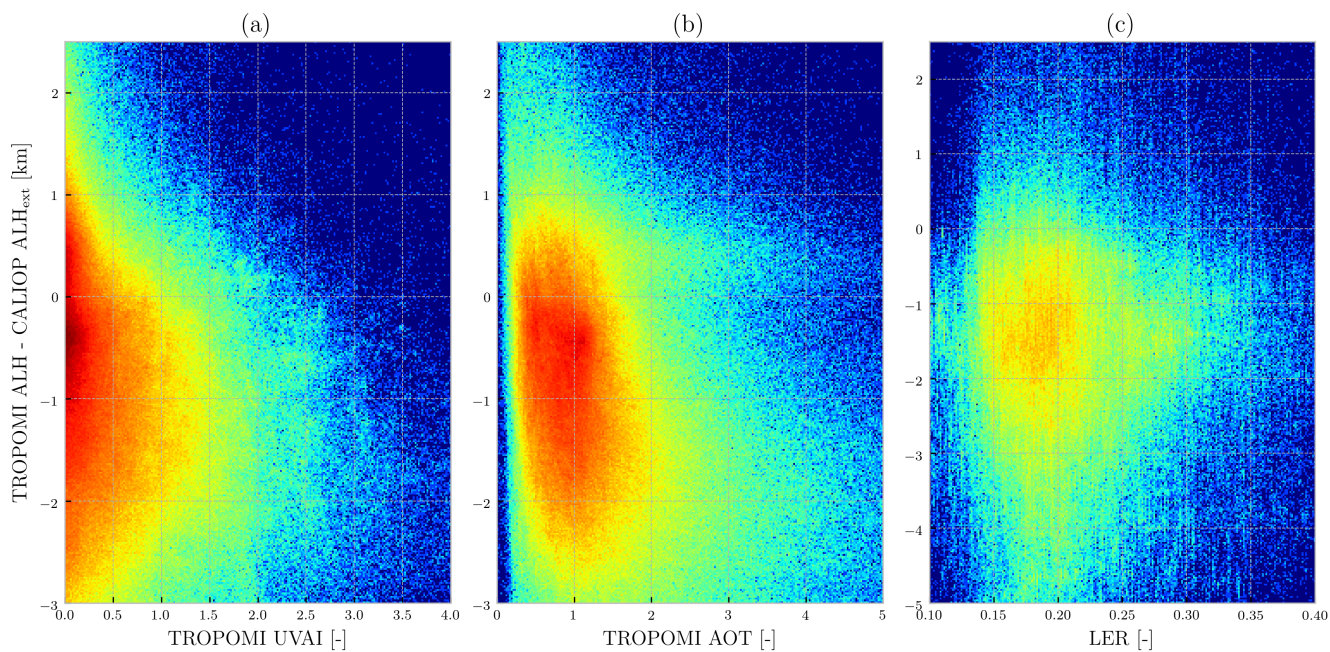


Figure 4. Scatter density plots of the difference between TROPOMI ALH and CALIOP ALH_{ext} as a function of (a) TROPOMI UVAI, (b) TROPOMI AOT and (c) GOME-2 LER for the oxygen A-band used for the TROPOMI retrievals for cases over land (with a minimum surface albedo of 0.1). The colors represent density of plots. The y axis is optimised for each plot. The data is filtered in the same fashion as in Figure 2, with data over the ocean and land combined for plots (a) and (b), and data only over land for plot (c).

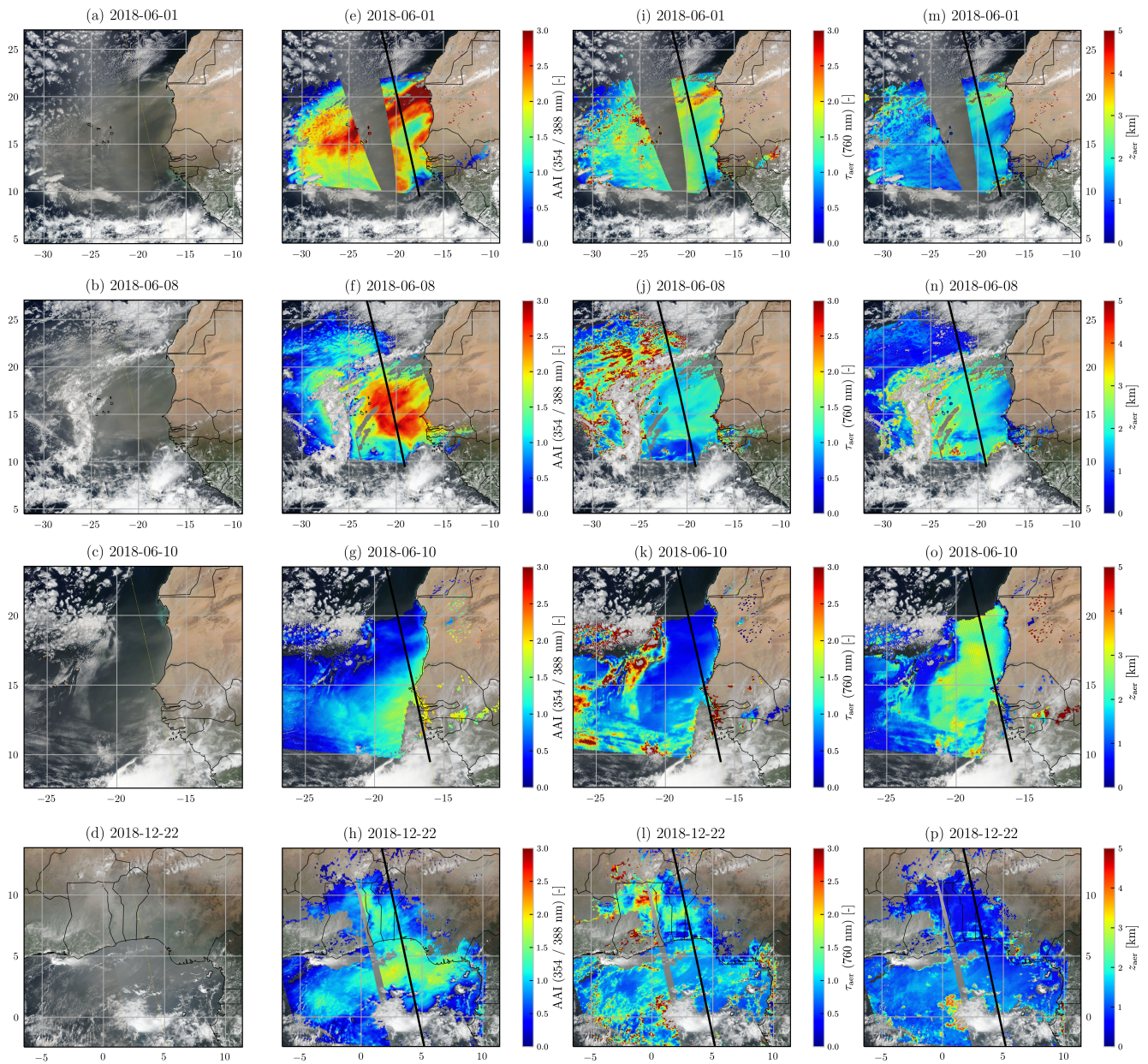


Figure 5. **1st column:** Corrected reflectance for the four selected cases as measured by the Suomi NPP/VIIRS imager. The yellow line represents the CALIOP ground track. **2nd column:** The TROPOMI level-2 UV aerosol index product. The black line passing through the TROPOMI level-2 retrievals on this plot represents the ground track of the CALIPSO mission. **3rd column:** Retrieved AOT from TROPOMI. **4th column:** Operational TROPOMI ALH.

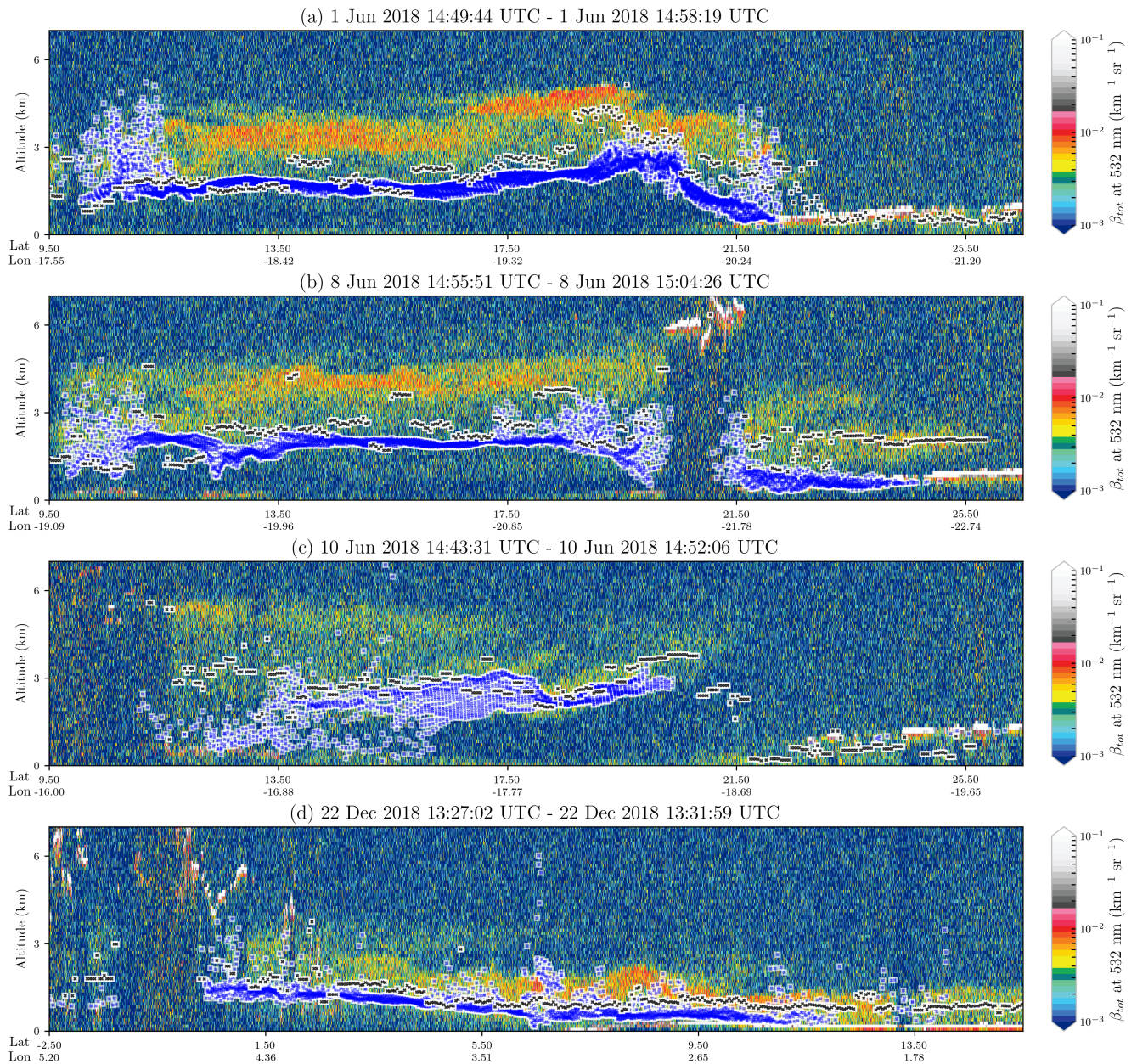


Figure 6. CALIOP level-1 backscatter curtain plots for measurements in the 532 nm channel for the four selected cases in Figure 5. The blue markers (crosses over a white box) represent co-located TROPOMI ALH retrievals within 100 km of each CALIOP profile present in this plot. The black markers (crosses over a white box) represent the CALIOP weight aerosol heights as computed using Equation 2. TROPOMI data that are either in sun-glint region or cloud contaminated are removed (cloud detection is done using the cloud_warning flag from Table 1).

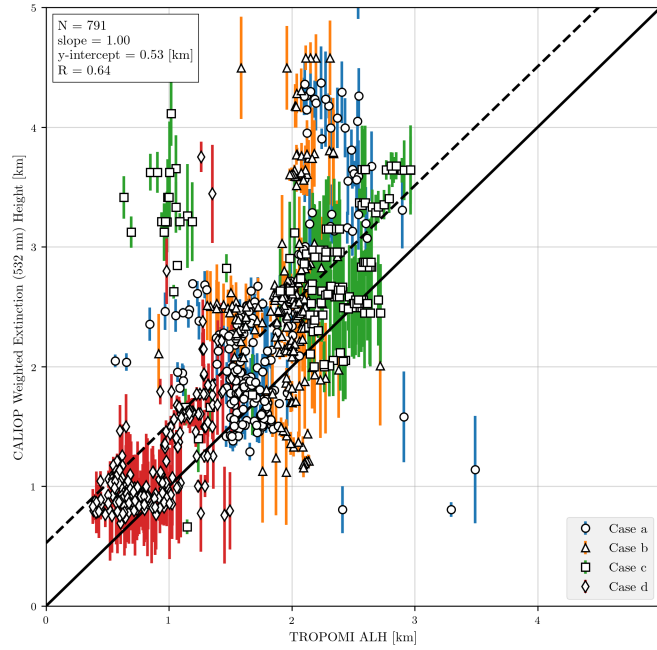


Figure 7. Comparison between the CALIOP weighted extinction heights (y-axis) calculated using Equation 2 and plotted in Figure 6, against averaged TROPOMI ALH (x-axis). The blue lines represent the standard deviation of the TROPOMI heights in the averaging pool, and the markers represent the mean TROPOMI ALH for each CALIOP ALH_{ext}. The dashed black line marks the fit between CALIOP ALH_{ext} and TROPOMI ALH. The solid black line is a neutral line between the x and the y axes. The legend in the bottom right corner describes the different markers used for the different cases. The colors represent the cases — blue for case a, yellow for case b, green for case c and red for case d.

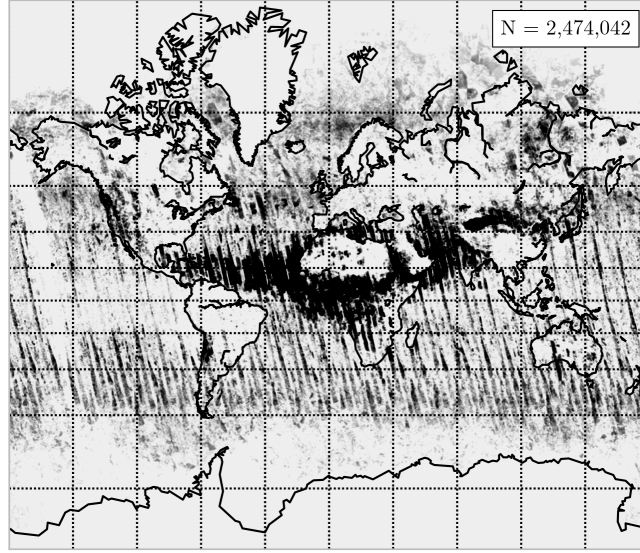


Figure 8. A map of all TROPOMI-CALIOP collocations considered for Figure 2 (data filtering discussed in Appendix A).

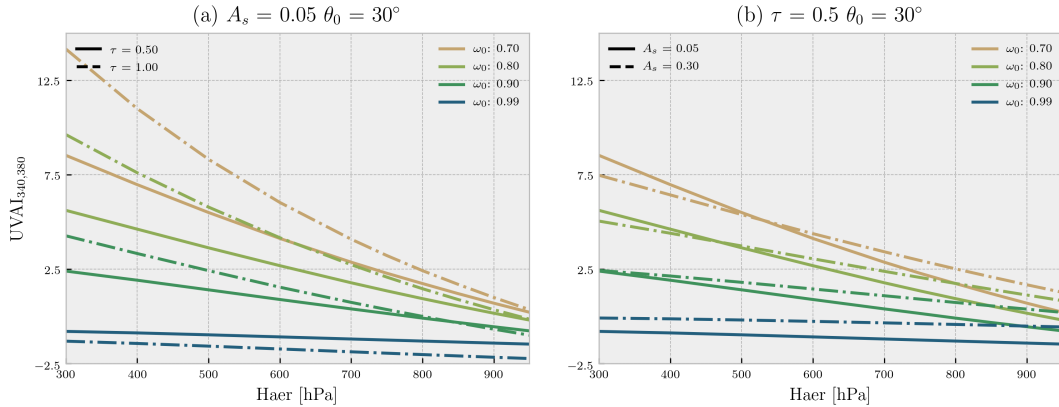


Figure 9. Sensitivity analysis of UV aerosol index to show the influence of different aerosol properties on the UVAI. The aerosols in these analyses have a Henyey-Greenstein scattering phase function with an asymmetry factor of 0.7, an angstrom exponent of 1.0, the viewing zenith angle is 0° , the solar azimuth angle and the viewing azimuth angles are 0° and 60° respectively, the surface pressure is 1013 hPa, and for this specific case, the solar zenith angle θ_0 is 30° . The y-axis is the UVAI for 340 nm and 380 nm, whereas the x-axis is the height of the geometric centroid of the aerosol layer in hPa (Haer). The legend in each of the plots describe the different configurations chosen for these sensitivity analyses. **(a)** looks into the sensitivity of UVAI with a fixed surface albedo of 0.05, and **(b)** does the same for a fixed AOT of 0.5.